Nanoscale

PAPER

View Article Online
View Journal | View Issue



Cite this: *Nanoscale*, 2014, **6**, 13154

# Synthesis of cubic and spherical Pd nanoparticles on graphene and their electrocatalytic performance in the oxidation of formic acid

Sudong Yang,[a,b,c] Chengmin Shen,[a] Yuan Tian,[a] Xiaogang Zhang*[b] and Hong-Jun Gao*[a]

Received 31st July 2014,
Accepted 31st August 2014

DOI: 10.1039/c4nr04349a

www.rsc.org/nanoscale

Single-crystal palladium nanoparticles (NPs) with controllable morphology were synthesized on the surface of reduced graphene oxide (RGO) by a novel procedure, namely reducing palladium acetylacetonate [Pd(acac)$_2$] with the *N*-methylpyrrolidone (NMP) solvent in the presence of poly(vinylpyrrolidone) (PVP). The resulting Pd nanocrystals (8 nm in diameter) were uniformly distributed on the RGO. A possible formation mechanism is discussed. The electrocatalytic performance of Pd nanocrystal/RGO catalysts during formic acid oxidation was investigated, which revealed that the cubic Pd/RGO catalyst performed significantly better than the spherical Pd/RGO catalyst. The shape of Pd nanocrystals on the surface of graphene nanosheets can be easily controlled *via* tuning the synthesis parameters, resulting in tunable catalytic properties. Moreover, this method can be easily extended to fabricate other noble metal nanostructures.

## 1. Introduction

The morphology-controlled synthesis of nanostructures has attracted considerable attention because the size and morphology of most nanostructures strongly affect their chemical and physical properties.[1–4] Palladium, one of the most-studied materials, has attracted considerable interest for its applications in numerous fields[5–9] such as fuel-cell technology. Recently, Pd nanomaterials were also used as electrocatalysts for the electrooxidation of formic acid, and the results revealed that Pd is a good electrocatalyst for direct formic acid fuel cells (DFAFCs), making them less vulnerable to CO poisoning than those that contain Pt catalysts.[10–12] Because the catalytic efficiency highly depends on both the morphology and size of the Pd nanomaterials, much effort has been expended toward the size- and morphology-controlled synthesis of Pd nanostructures and the characterization of their catalytic activity.[13–15] It has been found that certain shapes of Pd nanostructures exhibit superior catalytic action.[13] In particular, cubic Pd nanoparticles (NPs) have drawn attention because of their excellent electrocatalytic activities.[14] Studies of formic acid oxidation have indicated that the (100) facet of Pd shows the highest catalytic activity among the three low-index facets, implying that these (100)-faceted Pd cubic catalysts are more practical for fuel cell applications.

To prevent aggregation and to maximize the electrocatalytic activity of Pd NPs, a suitable carbon support is necessary to disperse these nanostructures. Conventional carbon supports for electrocatalysts include XC-72 carbon black (~250 m$^2$ g$^{-1}$) and carbon nanotubes (typically only ~200 m$^2$ g$^{-1}$). Among the carbon materials, graphene has recently attracted tremendous attention and holds great promise for advanced fields.[16–19] Because of its huge surface area (calculated value: 2630 m$^2$ g$^{-1}$), high electrical conductivity, and excellent catalytic activity,[20,21] graphene is considered a promising candidate as a material to support Pd NPs for applications in DFAFCs.[22–25] The reduction of graphene oxide (GO) has been considered promising for high-yield preparation of graphene. However, the graphene sheets that are primarily prepared by the chemical reduction of graphite oxide easily aggregate irreversibly into 3D agglomerates due to strong sheet-to-sheet van der Waals interactions. Aggregation of graphene sheets not only negates the advantages of high-surface-area graphene, but also obstructs their dispersion in catalyst ink. In addition, the even distribution of uniform sized metal NPs onto graphene by synchronous chemical reduction of metal precursors and GO is difficult. Furthermore, most of the previous studies have primarily involved spherical Pd NPs or NPs with an undetermined

[a]*Beijing National Laboratory for Condensed Matter Physics, Institute of Physics, Chinese Academy of Sciences, Beijing 100190, P. R. China. E-mail: hjgao@ iphy.ac.cn, azhangxg@163.com*
[b]*College of Material Science and Engineering, Nanjing University of Aeronautics and Astronautics, Nanjing 210016, P. R. China*
[c]*Laboratory of Environmental Science and Technology, Xinjiang Technical Institute of Physics & Chemistry, Chinese Academy of Sciences, Urumqi, 830011, P. R. China*

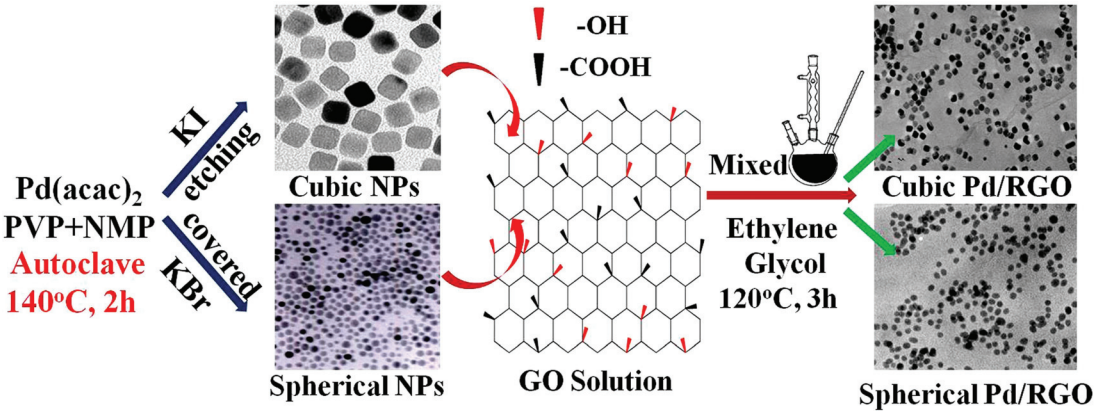


**Fig. 1** Illustration of the synthesis procedure for the cubic Pd/RGO and spherical Pd/RGO catalysts. The two-step process: (a) cubic and spherical Pd NPs were synthesized using a solvothermal method; (b) Pd NPs were dispersed on the graphene oxide solution to form Pd/RGO.

shape. Therefore, the fabrication of uniformly sized Pd nanocubes/graphene composite catalysts with high dispersion remains a challenge. To minimize these disadvantages, the introduction of highly dispersed and uniformly sized Pd NPs onto graphene, in such a way that it would retain the very large surface area of the graphene, is desirable. Pd NPs could serve as a "separator" material with respect to the separation and stabilization of reduced graphene oxide (RGO) sheets.[26]

In this paper, we report an effective strategy for controlling the morphology and dispersion of Pd NPs supported on graphene using a two-step process. High dispersion of Pd nanocubes and spherical NPs supported on graphene is achieved through a chemical reduction, which can be divided into two steps (Fig. 1). In the first step, we used a solvothermal method for the morphology-controlled synthesis of palladium nanocubes in the presence of KI and spherical nanoparticles without KI from an *N*-methylpyrrolidone (NMP) solution system. In the second step, with the addition of GO and a reducing reagent, cubic Pd/GO and spherical Pd/GO were further transformed into cubic Pd/RGO and spherical Pd/RGO. The cubic Pd/RGO catalyst showed far better catalytic activity and stability toward formic acid electro-oxidation than the spherical Pd/RGO catalyst. As far as we know, there are no reports on uniformly sized and highly dispersed Pd nanocubes supported on graphene, prepared *via* a two-step chemical reduction.

## 2. Experimental section

### 2.1 Materials

Pd(II) acetylacetonate ($Pd(acac)_2$, 99%) was purchased from Sigma Aldrich. Poly(vinylpyrrolidone) (PVP, MW = 10 000, AR) was purchased from Acros. KI was purchased from Beijing Chemistry Reagent (Beijing, China). *N*-Methylpyrrolidone (NMP) and graphite power (99.99%) were purchased from Sinopharm Chemical Reagent (Shanghai, China). The water used in all experiments was ultrapure with a resistivity of 18.2 MΩ cm. All reagents were used as received without further purification.

### 2.2 Synthesis of the Pd nanocubes and spherical Pd nanoparticles

Synthesis of Pd nanocubes: $Pd(acac)_2$ (50.0 mg), PVP (160.0 mg) and KI (143.2 mg) were mixed together in NMP (12 ml). The resulting homogeneous brown solution was transferred to a Teflon-lined stainless-steel autoclave. The sealed vessel was then heated at 140 °C for 2 h before it was cooled to room temperature. The black nanoparticles were precipitated with acetone, separated using a centrifuge, and further purified using an ethanol–acetone mixture to remove excess NMP and surfactants. The final black product could be easily redispersed in polar solvents, such as ethanol and water, to yield a homogeneous solution. The procedure for the preparation of the spherical Pd nanoparticle composites was similar to that used for the Pd nanocubes, except that KBr was used instead of KI.

The graphite oxide was synthesized from natural graphite powder according to a method reported in the literature.[25] In a typical procedure for the preparation of cubic Pd/RGO hybrids, 4.3 mg of Pd nanocubes in 3 ml of DI water and 10 mg of GO were added to 20 ml of ethylene glycol in a 50 ml flask. The mixture was first ultrasonically mixed for 2 h to ensure that GO was uniformly dispersed in the ethylene glycol–water solution. The reduction reaction was then performed in the flask at 120 °C for 3 h under constant stirring. The cubic Pd/RGO hybrids were finally separated by centrifugation and were subsequently washed with deionized water several times. For comparison, the same procedure was followed for the synthesis of spherical Pd/RGO composites.

### 2.3 Characterization

X-ray diffraction (XRD) analysis was performed on a Rigaku D/MAX 2400 X-ray diffractometer equipped with a Cu Kα radiation ($\lambda$ = 0.15418 nm) source. X-ray photoelectron spectroscopy (XPS) was performed on an ASTM E1829-02 system.

The analysis of the composition of the catalyst was performed on a Thermo IRIS Intrepid II inductively coupled plasma atomic emission spectrometry (ICP-AES) system. The morphology of the samples was investigated using transmission electron microscopy (TEM, JEOL JEM-2100). The crystallinity of the material was observed using high resolution TEM (JEOL JEM-2010).

### 2.4 Preparation of the electrodes

Glassy carbon (GC) electrodes, 5 mm in diameter (electrode area: 0.196 $cm^2$) and polished with 0.05 μm alumina to a mirror finish before each experiment, were used as substrates for the catalysts. The catalysts were washed with 0.5 M NaOH and isopropanol to remove excess surfactant. For the electrode preparation, 3 mg of the catalyst was typically added to 0.5 ml of 0.05 wt% Nafion–ethanol solution, and the mixture was subsequently mixed for 1 h with ultrasonication to ensure uniform dispersion. A measured volume (30 μl) of this mixture was dropped from a microsyringe onto the top surface of the GC electrode. The as-obtained catalyst-modified GC electrode was used as the working electrode in our experiments.

### 2.5 Electrochemical measurements

All electrochemical measurements were performed on a CHI 660D electrochemical workstation using a three-electrode test cell. A conventional three-electrode system was used with a modified GC electrode as the working electrode, Pt foil as the counter electrode and an Ag/AgCl (saturated KCl) electrode as the reference electrode. All electrolytes were deaerated by bubbling $N_2$ for 20 min and were protected with a nitrogen atmosphere during the entire experimental procedure. All experiments were performed at a temperature of 25 ± 1 °C.

## 3. Results and discussion

The Pd nanocubes were prepared in the presence of PVP and KI using NMP as the solvent. The morphological structure, the particle size, and the dispersion of Pd nanocubes were investigated using TEM. Fig. 2a and b show typical TEM images of as-prepared Pd nanocubes with an average size of 8 nm. The low-magnification TEM image shows that Pd nanocubes have well-defined shapes with a narrow size distribution. The HRTEM image of a single Pd nanocube (Fig. 2c) shows lattice fringes with an interfringe distance of approximately 1.9 Å, which is close to the {200} interplane distance of face-centered-cubic (fcc)-structured Pd. This result demonstrates that the {100} surface of the fcc-structured Pd nanocubes is selectively exposed.[27] The HRTEM image also confirms that the nanocubes are single-phase Pd. The single-crystalline nature of the nanocubes is evident from the appearance of continuous lattice fringes oriented in the same direction across the cube.[28] The selected area electron diffraction (SAED) of Pd nanocubes clearly shows the typical fcc structure with diffraction rings of the {111}, {200}, {220} and {311} surfaces, which indicates the highly crystalline nature of the Pd nanocubes (Fig. 2d).

To elucidate the composition of the Pd nanocubes, XPS was used to investigate the interaction between Pd atoms, PVP

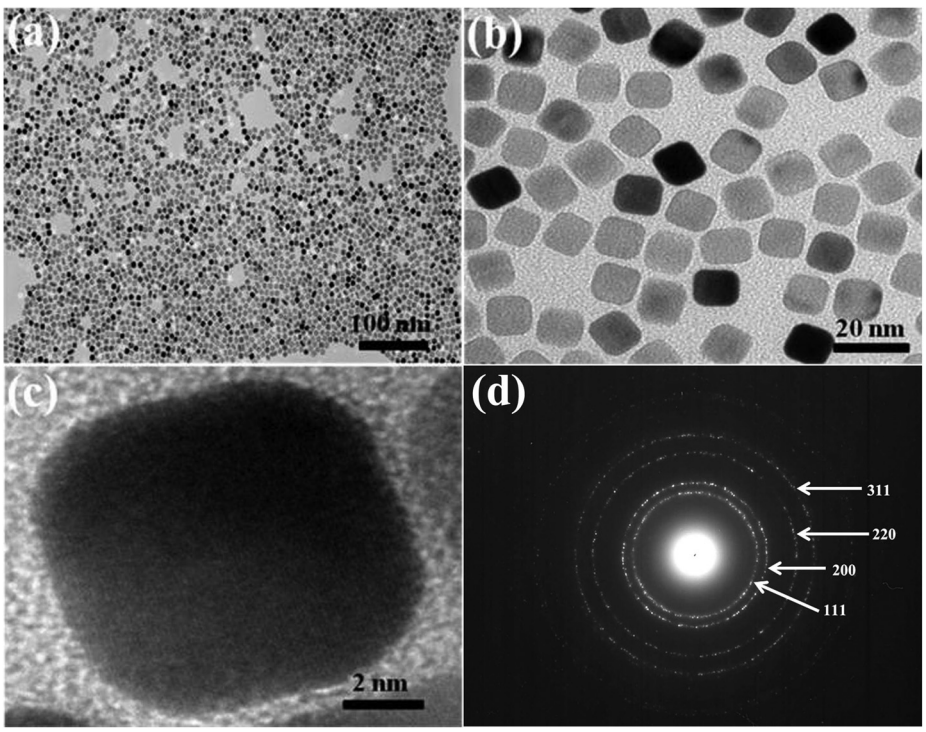


Fig. 2 TEM images of Pd nanocubes with an average size of 8 nm. (a, b) Low-magnification images of nanocubes; (c) HRTEM image of Pd nanocubes; (d) SAED pattern of Pd nanocubes.

 

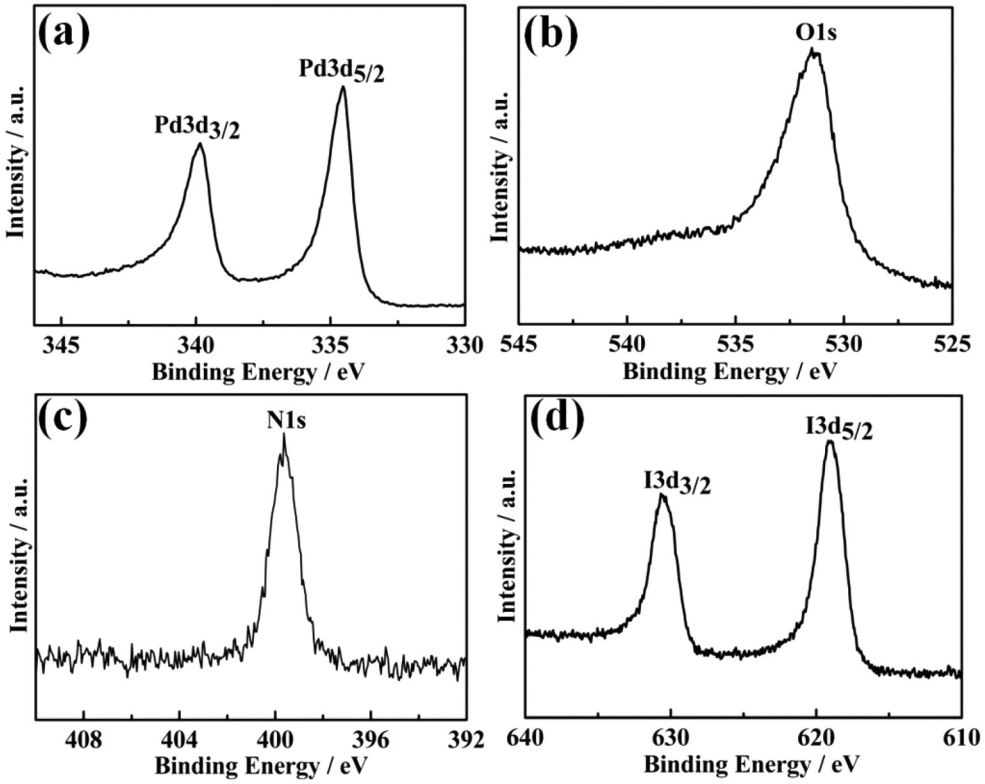


**Fig. 3** X-ray photoelectron spectra of Pd nanocubes. (a) Binding energy of Pd 3d; (b) binding energy of O 1s; (c) binding energy of N 1s; and (d) binding energy of I 3d.

molecules, and KI during the formation of Pd nanocubes. Fig. 3 shows the XPS spectra of the Pd nanocubes. In Fig. 3a, the XPS spectrum of Pd shows double peaks with binding energies of 334.59 eV and 339.83 eV. These peaks correspond to Pd $3d_{5/2}$ and Pd $3d_{3/2}$, respectively. A comparison of this spectrum to the standard spectra of metal $Pd^0$ (ref. 27) reveals that the binding energies of Pd nanocubes slightly decreases (from 335.1 eV to 334.59 eV and from 340.4 eV to 339.83 eV). The energy banding of O 1s in the PVP-capped Pd NPs shifted to higher values, *i.e.*, from 530.55 eV to 531.45 eV (see Fig. 3b). These results indicate that the PVP can be adsorbed onto the surface of Pd particles by the bonding between Pd and O. The adsorption of oxygen atoms onto the Pd nanocubes will induce partially positive charges on the surface of the nanocubes. In contrast, for the N 1s peak, no obvious shift is observed in the spectra of the PVP-coated Pd nanocubes (Fig. 3c), which indicates that the chemical environment around nitrogen atoms does not change. This fact indicates that nitrogen atoms do not interact with Pd atoms directly. The I $3d_{5/2}$ and I $3d_{3/2}$ binding energies are 618.98 and 630.68 eV, respectively (see Fig. 3d), which are very close to the literature values for KI (618.6 and 630.1 eV). The small shift of I 3d peaks is attributed to the binding of I to the Pd surface.[29,30] These results confirm that the PVP can be adsorbed onto the surface of Pd particles by the bonding between Pd and O and that I can be adsorbed onto the surface of Pd nanocubes by chemisorption.

Reaction temperature played a key role in controlling the NPs' shape. In our experiment, PVP and NMP were not only selected as the surfactant and the solvent, but also simultaneously served as mild reducing agents. KI is an etching agent for Pd NPs. Fig. 4 shows TEM images of Pd NPs prepared at different reaction temperatures. At lower reaction temperature (<120 °C), the rate of the reduction reaction is slowed down and cannot provide enough energy for the Ostwald ripening process and anisotropic growth. So, Pd NPs with non-uniform shapes are formed at lower temperature (Fig. 4a). In contrast, a higher reaction temperature (>160 °C) results in a faster reduction rate and growth process. On the other hand, the surfactant molecule capped on the surface of Pd NPs becomes unstable at higher temperatures, which leads to significant aggregation of Pd nanocubes (Fig. 4b). From Fig. 4c, it can be seen that monodisperse Pd nanocubes with an edge length of 8 nm were obtained at 140 °C.

XPS analysis indicated that the PVP can be capped on the surface of Pd NPs by the bonding between Pd and O, while iodide ions can be adsorbed onto the surface of a Pd nanoparticle by chemisorption. In this synthetic system, the use of PVP and $I^-$ ions can stabilize Pd {100} facets and assist in the formation of Pd nanocubes. Therefore, the shape-control of Pd NPs can be achieved through tuning the molar ratio of KI to PVP. The rectangle-shaped Pd NPs were observed at lower amount of KI, indicating that the etching rate of $I^-$ was lower and the NPs were capped by PVP molecules (Fig. 5a).

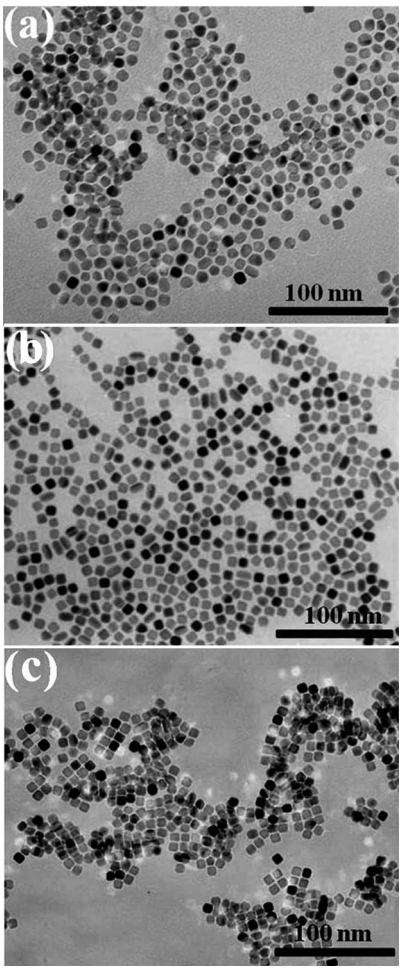


Fig. 4 TEM images of Pd NPs prepared at different reaction temperatures: (a) 120 °C, (b) 140 °C, and (c) 160 °C. The results indicate that monodisperse Pd nanocubes were obtained at 140 °C.

The shape of Pd NPs gradually changed to a uniform cubic morphology with increasing the amount of KI. The narrow size distribution, mono-dispersion and typical cubic shape of Pd NPs were achieved at a KI : PVP molar ratio of 1.4. For more KI, the as-prepared NPs took various shapes, including small spheres, little cubes and irregular rectangles. This occurred because the etching ability of $I^-$ and the etching rate both increased. We found that continually increasing the amount of KI led to aggregation of Pd NPs due to decreased adsorption of PVP molecules on the Pd NPs' surfaces.

Results from our reaction media show that the acetylacetonate precursors and iodide ions play an important role in the formation of the monodisperse palladium nanocubes. The addition of iodide ions to the $[Pd(acac)_2]$ mixture results in $[PdI_4]^{2-}$ becoming the dominant precursor. In NMP, we found evidence that the reduction of $[PdI_4]^{2-}$ is more favorable than $[Pd(acac)_2]$. In this synthetic system, the use of PVP and $I^-$ can stabilize Pd {100} facets and therefore assist in the formation of Pd nanocubes. As reported in the literature, bromide can cover the surface of Pd NPs due to its strong binding to the Pd surface when KI is used instead of KBr. The bromide ions' chemisorption on the surface of Pd resulted in surface protection and the product mainly consisted of spherical NPs.[29,30]

The morphologies of the graphene-nanosheet-supported cubic Pd and spherical Pd NPs were also characterized using TEM. Fig. 6 shows TEM images of the cubic Pd/RGO composites and the spherical Pd/RGO composites. The TEM image of the cubic Pd/RGO in Fig. 6a shows that the reduced GO did not degrade the quality of the Pd nanocubes formed on the RGO support and that the Pd nanocubes were of uniform size and were well-dispersed over the support surface with greater retention of the nanocube characteristics. As shown in Fig. 6b, spherical Pd nanoparticles were deposited onto the surface of RGO with greater retention of the spherical characteristics of the NPs. Based on the TEM results, we note that the sizes of both the Pd nanocubes and the Pd spherical nanoparticles remain unchanged during the GO reduction process.

The crystal phases of the Pd nanocubes, the cubic Pd/RGO composite and the spherical Pd/RGO composite were also characterized using X-ray diffraction (XRD). Fig. 7a shows the XRD pattern of the Pd nanocubes. Reflection peaks can be observed at 40.1°, 46.7°, 67.8°, 82.1°, and 86.4°, which correspond to the (111), (200), (220), (311) and (222) planes of Pd, respectively. The reflection peaks are consistent with an fcc crystalline structure of bulk Pd (JCPDS, card no. 46-1043). An average diameter of 7.5 nm was estimated from the Scherrer equation, and this result is consistent with the TEM analysis results. The intensity ratio of (111) to (200) peaks is significantly lower than the standard value calculated from the JCPDS data (from 2.38 decreased to 1.54), which indicates that the (100) planes dominate in the Pd nanocubes. The XRD pattern of Pd/RGO in Fig. 7b shows the as-prepared Pd nanocubes dispersed on the surface of GO to form cubic Pd/RGO composites. The diffraction peaks for cubic Pd/RGO are the same as those observed for the Pd nanocubes, indicating that the crystal structure of Pd nanocubes did not change after the cubes were deposited on the RGO. We found that the typical (002) diffraction peak of RGO shifts to a higher angle after the reduction by ethylene glycol. This shift could be attributable to the fact that GO is partially reduced to graphene and restacked into an ordered crystalline structure. From Fig. 7c, the diffraction peaks at around 40.0°, 67.3° and 80.8° correspond to the (111), (220) and (311) planes of the fcc lattice, indicating that the spherical Pd NPs have a fcc crystal structure. In contrast to the cubic Pd/RGO, it can be seen that the diffraction peaks of spherical Pd/RGO are broader and the intensity of peaks is decreased somewhat. On the other hand, the diffraction angles of spherical Pd/RGO composites shift toward lower values. These results indicate that the spherical Pd NPs are typical small particles in this regard and have a polycrystalline structure.[31–33]

The cubic Pd/RGO composite and the spherical Pd/RGO composite were then evaluated as catalysts for the electro-oxidation of formic acid. The cubic Pd/RGO and the spherical Pd/RGO were synthesized by very similar methods (except for the different etching agents), so their surfaces should be capped by similar residual chemical groups. Therefore, we could

 

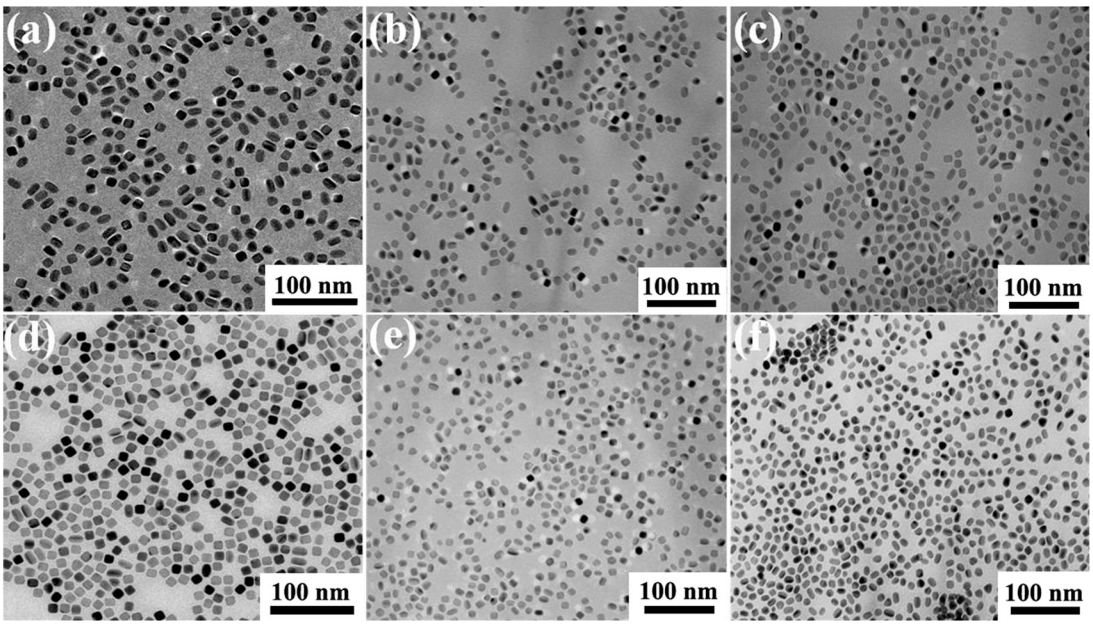


**Fig. 5** TEM images of Pd NPs prepared at different molar ratios of KI to PVP: (a) 0.6, (b) 1.0, (c) 1.2, (d) 1.4, (e) 1.6, and (f) 2.0. The narrow size distribution, monodispersion and typical cubic shape of Pd NPs were achieved at the molar ratio of 1.4.

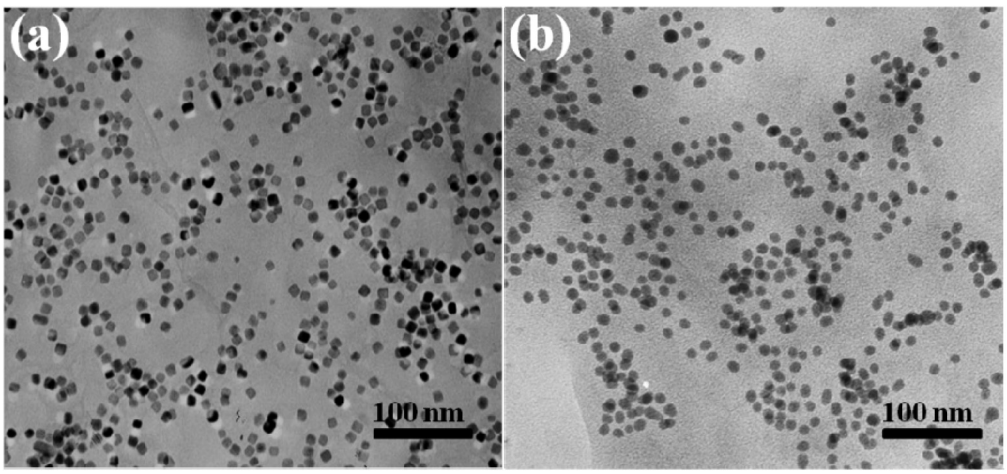


**Fig. 6** TEM images of (a) cubic Pd/RGO and (b) spherical Pd/RGO. The results indicate that Pd NPs were uniformly dispersed on the surface of RGO.

directly compare their activities to determine the influence of atomic structure on the surface. The electrochemically active surface area (ECSA) can provide important information on the available active sites of catalysts. Hydrogen adsorption/desorption is commonly used to evaluate the ECSA in an electrochemical setup. Fig. 8a shows the cyclic voltammograms of glassy carbon electrodes coated with the different electrocatalyst films in 0.25 M $H_2SO_4$ solution at a scan rate of 50 mV $s^{-1}$. The integrated peak area under the curve gives the amount of hydrogen desorbed and provides an estimation of the ECSA. The integrated area of the hydrogen adsorption and desorption peaks for the cubic Pd/RGO electrode is larger than that of the spherical Pd/RGO electrodes. These results reveal that cubic Pd/RGO contains more active sites and exhibits a larger ECSA.

The amount of Pd in different samples was evaluated using ICP-AES. The ICP-AES measurements reveal that the metal loadings of the cubic Pd/RGO and the spherical Pd/RGO are 31.1 and 31.6 wt%, respectively. The oxidation currents in the cyclic voltammograms and the chronoamperometry tests were normalized relative to the weight of the catalysts in the electrode to allow further comparison of the activities of the two catalysts. Their catalytic activity toward formic acid oxidation was investigated. Fig. 8b shows the cyclic voltammograms of the electrodes coated with the cubic Pd/RGO electrocatalyst or with the spherical Pd/RGO electrocatalyst, immersed in a

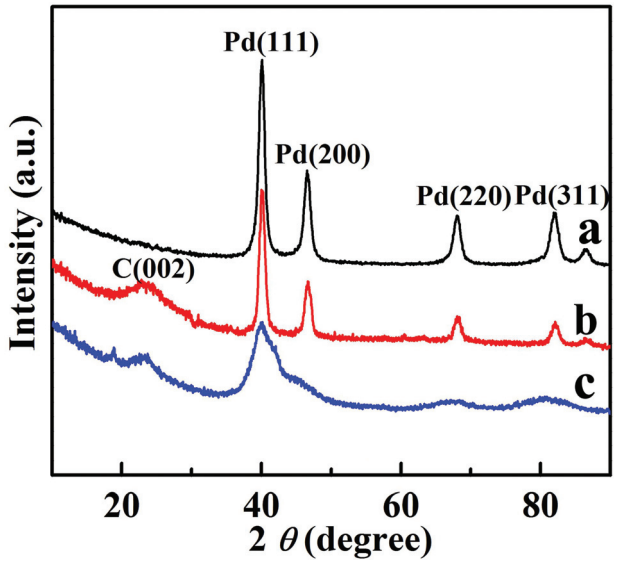


Fig. 7 XRD patterns of Pd nanocubes (a), cubic Pd/RGO (b), and spherical Pd/RGO (c); the patterns indicate that Pd nanocubes and spherical NPs have been deposited onto the surface of RGO.

0.25 M HCOOH and 0.25 M $H_2SO_4$ mixed solution at room temperature. The potential was scanned from −0.2 to 0.8 V *vs.* Ag/AgCl at a scan rate of 50 mV $s^{-1}$. In the positive scan, the first oxidation peak for the cubic Pd/RGO catalyst, observed at 0.11 V, is assigned to the oxidation of formic acid. As is evident in the voltammogram, the cubic Pd/RGO catalyst exhibits an especially high current density compared with that of the spherical Pd/RGO. The cubic Pd/RGO catalyst exhibits better electro-oxidation activity toward formic acid than the spherical Pd/RGO. This result could be attributed to the high activity resulting from the uniform size and excellent dispersion of the Pd nanocubes on the graphene. This result can also be explained by the abundance of {100} facets on the cubic Pd NPs, absent from the spherical Pd NPs, because these facets are highly active toward formic acid oxidation.[34] These results indicate that the reactivity and selectivity of Pd NPs can be tailored through adjustment of their morphology, which determines the structure of the crystallographic facets exposed on the surfaces of a nanocrystal and impact its potential behavior.

The importance of catalyst stability in fuel-cell applications is well known. The electrochemical stability of the two nanohybrids during formic acid oxidation was also investigated using chronoamperometric techniques. Fig. 8c shows the current–time curves of the cubic Pd/RGO and spherical Pd/RGO electrocatalysts recorded at 0.1 V. The residual current density after 3600 s at the cubic Pd/RGO nanohybrids is 0.85 mA $mg^{-1}$, which is 4.5 times that at the spherical Pd/RGO nanohybrids (0.2 mA $mg^{-1}$). This result further confirms that the

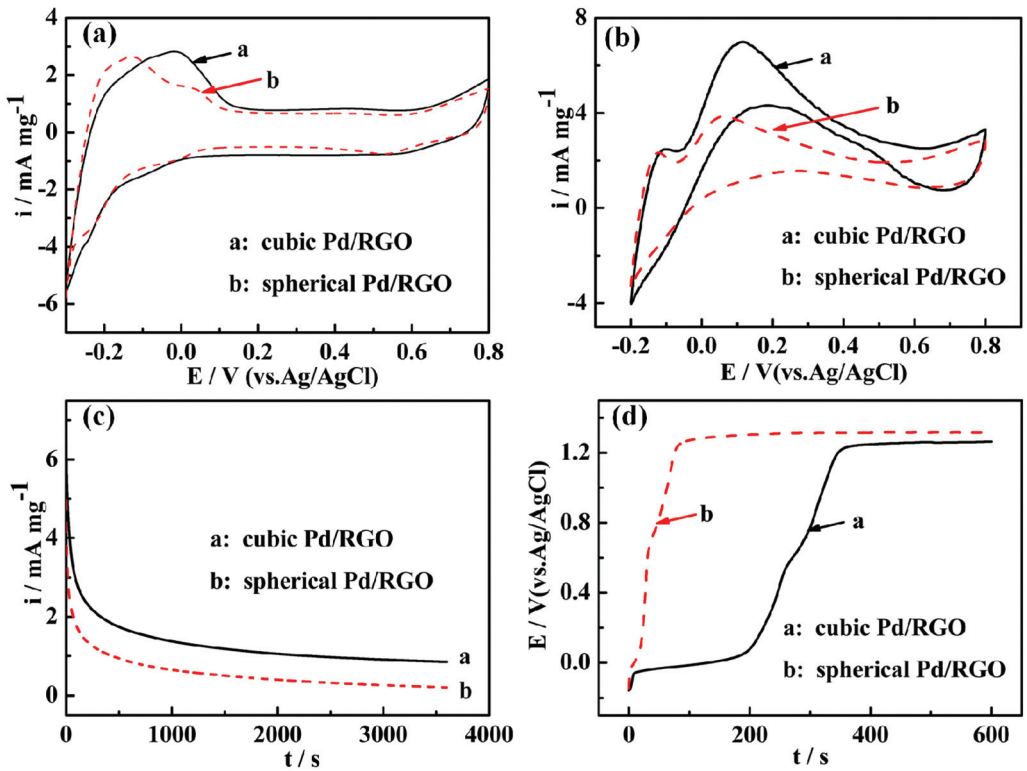


Fig. 8 (a) Cyclic voltammograms of different catalysts in 0.25 M $H_2SO_4$ solution at a scan rate of 50 mV $s^{-1}$; (b) cyclic voltammograms of formic acid oxidation on the catalysts in a 0.25 M $H_2SO_4$ and 0.25 M HCOOH mixed solution at a scan rate of 50 mV $s^{-1}$; (c) chronoamperometry curves of different catalysts in a 0.25 M $H_2SO_4$ and 0.25 M HCOOH mixed solution at 0.1 V; and (d) chronopotentiometric curves of different catalysts in a 0.25 M $H_2SO_4$ and 0.25 M HCOOH mixed solution with an anodic current of 1 mA.

 

cubic Pd/RGO nanohybrids are more electrochemically stable during formic acid oxidation than are the spherical Pd/RGO nanohybrids, as observed in the related CV investigation.

Chronopotentiometry is a useful method to study the resistance to poisoning of catalysts during formic acid oxidation. All of the catalysts were characterized using chronopotentiometry and, as is evident from the results in Fig. 8d, the electrode potential increased gradually for several hundred seconds and then increased to a higher potential. The reason for this increase is as follows: during the chronopotentiometric experiment, the poisonous species $CO_{ads}$ generated from formic acid oxidation accumulate on the surface of the electrocatalyst and reduce its electrocatalytic activity. The potential must be increased to satisfy the applied anodic current density. When the electrocatalyst becomes heavily poisoned, the formic acid oxidation reaction cannot continue. To satisfy the applied anodic current density, the potential must be increased.[35] Here, the time ($T$) at which the electrode potential increases to a higher potential is introduced to judge the anti-poisoning ability of the catalyst. Based on the corresponding data in Fig. 8d, the $T$ values increase in this order: cubic Pd/RGO catalysts (192 s) > spherical Pd/RGO catalysts (30 s). Obviously, the oxidation of formic acid on the cubic Pd/RGO electrode was relatively stable at low potentials. These results prove that the cubic Pd/RGO catalysts exhibit better electrocatalytic properties and better resistance to poisoning than do the spherical Pd/RGO catalysts, during formic acid oxidation.

A recent investigation showed that the slow adsorption of a "CO-like" intermediate might be principally responsible for the deactivation of Pd catalysts during formic acid oxidation.[36] Graphene sheets prepared through chemical reduction with EG are known to contain some residual oxygen groups. The remarkably strong anti-poisoning activity of the cubic Pd/RGO electrocatalyst has been found to be associated with the type and surface density of covalently bound oxygen-containing groups that remain on the RGO support. The presence of residual oxygen groups on the graphene support can promote the oxidation of adsorbed CO, $CO_{ads}$, on the active Pd sites *via* the mechanism described in the following equations and in the schematic of Fig. 9:[37]

$$RGO + H_2O \rightarrow RGO\text{-}(OH)_{ads} + H^+ + e^- \text{ Forward scan} \quad (1)$$

$$Pd\text{-}CO_{ads} + RGO\text{-}(OH)_{ads} \rightarrow CO_2 + Pd + RGO + H^+ + e^- \text{ Reverse scan} \quad (2)$$

The dissociative adsorption of water molecules on the RGO support creates $RGO\text{-}(OH)_{ads}$ surface groups adjacent to the Pd NPs (eqn (1)). The $RGO\text{-}(OH)_{ads}$ surface groups readily oxidize $CO_{ads}$ groups on the peripheral Pd atoms (eqn (2)). The hydrophilic nature of RGO promotes water activation and is the major driver of this mechanism.

All of these results reveal remarkable superiority in catalytic activity for the cubic Pd/RGO catalyst during formic acid oxidation compared to the carbon-black catalyst.[38] Based on these results, a more pronounced electrocatalytic activity can be induced by changing the structure of the nanocatalysts, which indicates that the effects of structure play a dominant role in catalytic performance. The enhanced electrocatalytic properties of our nanocubes may be attributed to the following three phenomena: (1) the high dispersion and size uniformity of Pd nanocubes on graphene result in high electrocatalytic activity toward formic acid oxidation. The most important aspect is that the cubic Pd NPs contain abundant {100} facets, which are absent from the spherical Pd NPs and are highly catalytically active toward formic acid oxidation. (2) The Pd nanocubes are a better "separator" material with respect to the separation and stabilization of graphene in the catalyst material. This is desirable not only to maximize the availability of the nanosized electrocatalyst surface area for electron transfer but also to provide better mass transport of reactants to the electrocatalyst. (3) A possible functional effect of the support may also occur during electrode reactions: the presence of residual oxygen groups on RGO plays a role in the removal of carbonaceous species from the adjacent Pd sites, which can promote the oxidation of formic acid.[37]

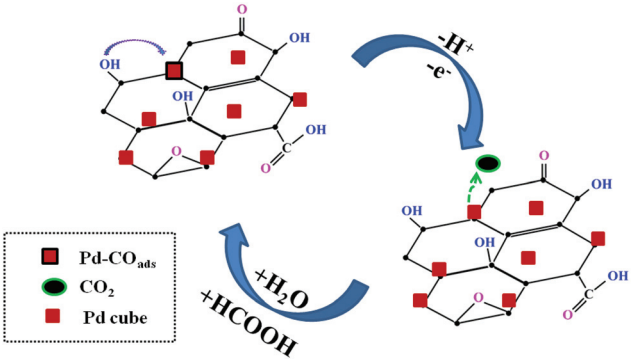


**Fig. 9** Schematic of the conversion of adsorbed $CO_{ads}$ species into $CO_2$ on the cubic Pd/RGO catalyst.

## 4. Conclusion

An effective two-step solvothermal synthesis route to Pd NPs with controllable morphology, supported on graphene, was developed. Both nanocubes and spherical NPs with uniform size (8 nm) were successfully prepared in the presence of KI and KBr, respectively. The unique architecture of these composites allows efficient use of the high surface area of graphene and effectively facilitates the formic acid oxidation process. The cubic Pd/RGO catalyst activity and stability toward formic acid oxidation were somewhat superior to the performance of the spherical Pd/RGO catalyst. Therefore, the present results suggest that this novel cubic Pd/RGO catalyst is a promising catalyst for DFAFCs.

## Acknowledgements

The work was supported by the National Natural Science Foundation of China (No. 61335006, 20873064, and 51302308) and the Program for Attracting High-level Talents in Xinjiang Uyghur Autonomous Region.

## References

1 Y. G. Sun and Y. N. Xia, *Science*, 2002, **298**, 2176.
2 C. Burda, X. Chen, R. Narayanan and M. A. El-Sayed, *Chem. Rev.*, 2005, **105**, 1025.
3 C. Wang, H. Daimon, T. Onodern, T. Koda and S. H. Sun, *Angew. Chem., Int. Ed.*, 2008, **47**, 3588.
4 Y. Wang, S. I. Choi, X. Zhao, S. F. Xie, H. C. Peng, M. F. Chi, C. Z. Huang and Y. N. Xia, *Adv. Funct. Mater.*, 2014, **24**, 131.
5 F. Favier, E. C. Walter, M. P. Zach, T. Benter and R. M. Penner, *Science*, 2001, **293**, 2227.
6 H. P. Liang, N. S. Lawrence, L. J. Wan, L. Jiang, W. G. Song and T. G. J. Jones, *J. Phys. Chem. C*, 2008, **112**, 338.
7 Y. Hatakeyama, M. Umetsu, S. Ohara, F. Kawadai, S. Takami, T. Naka and T. Adschiri, *Adv. Mater.*, 2008, **20**, 1122.
8 Y. Nishihata, J. Mizuki, T. Akao, H. Tanaka, M. Uenishi, M. Kimura, T. Okamoto and N. Hamada, *Nature*, 2002, **418**, 164.
9 D. Astruc, *Inorg. Chem.*, 2007, **46**, 1884.
10 Y. M. Zhu, A. Khan and R. I. Masel, *J. Power Sources*, 2005, **139**, 15.
11 S. D. Yang, X. G. Zhang, H. Y. Mi and X. G. Ye, *J. Power Sources*, 2008, **175**, 26.
12 Y. Liang, M. G. Zhu, J. Ma, Y. W. Tang, Y. Chen and T. H. Lu, *Electrochim. Acta*, 2011, **56**, 4696.
13 Y. J. Xiong and Y. N. Xia, *Adv. Mater.*, 2007, **19**, 3385.
14 M. S. Jin, H. Zhang, Z. X. Xie and Y. N. Xia, *Angew. Chem., Int. Ed.*, 2011, **50**, 7850.
15 Z. Q. Niu, Q. Peng, M. Gong, H. P. Rong and Y. D. Li, *Angew. Chem., Int. Ed.*, 2011, **50**, 6315.
16 A. K. Geim and K. S. Novoselov, *Nat. Mater.*, 2007, **6**, 183.
17 Y. Pan, H. G. Zhang, D. X. Shi, J. T. Sun, S. X. Du, F. Liu and H.-J. Gao, *Adv. Mater.*, 2009, **21**, 2777.
18 Y. Wang, Y. Y. Shao, D. W. Matson, J. H. Li and Y. H. Lin, *ACS Nano*, 2010, **4**, 1790.
19 L. Wang, C. G. Tian, H. Wang, Y. G. Ma, B. L. Wang and H. G. Fu, *J. Phys. Chem. C*, 2010, **114**, 8727.
20 D. R. Dreyer, S. Park, C. W. Bielawski and R. S. Ruoff, *Chem. Soc. Rev.*, 2010, **39**, 228.
21 M. Choucair, P. Thordarson and J. A. Stride, *Nat. Nanotechnol.*, 2009, **4**, 30.
22 X. M. Chen, G. H. Wu, J. M. Chen, X. Chen, Z. X. Xie and X. R. Wang, *J. Am. Chem. Soc.*, 2011, **133**, 3693.
23 S. D. Yang, J. Dong, Z. H. Yao, C. M. Shen, X. Z. Shi, Y. Tian, S. X. Lin and X. G. Zhang, *Sci. Rep.*, 2014, **4**, 4079.
24 H. Zhao, J. Yang, L. Wang, C. G. Tian, B. J. Jiang and H. G. Fu, *Chem. Commun.*, 2011, **47**, 2014.
25 S. D. Yang, C. M. Shen, Y. Y. Liang, H. Tong, W. He, X. Z. Shi, X. G. Zhang and H.-J. Gao, *Nanoscale*, 2011, **3**, 3277.
26 Y. C. Si and E. T. Samulski, *Chem. Mater.*, 2008, **20**, 6792.
27 H. Ding, X. Z. Shi, C. M. Shen, C. Hui, Z. C. Xu, C. Li, Y. Tian, D. K. Wang and H.-J. Gao, *Chin. Phys. B*, 2010, **19**, 106104.
28 X. Q. Huang, H. H. Zhang, C. Y. Guo, Z. Y. Zhou and N. F. Zheng, *Angew. Chem., Int. Ed.*, 2009, **48**, 4808.
29 Y. Xiong, H. Cai, B. J. Wiley, J. Wang, M. J. Kim and Y. N. Xia, *J. Am. Chem. Soc.*, 2007, **129**, 3665.
30 B. Wiley, Y. G. Sun and Y. Xia, *Acc. Chem. Res.*, 2007, **40**, 1067.
31 Y. Liu, C. Wang, Y. J. Wei, L. Y. Zhu, D. G. Li, J. S. Jiang, N. M. Markovic, V. R. Stamenkovic and S. H. Sun, *Nano Lett.*, 2011, **11**, 1614.
32 C. M. Shen, Y. K. Su, H. T. Yang, T. Z. Yang and H.-J. Gao, *Chem. Phys. Lett.*, 2003, **373**, 39.
33 C. W. Xiao, C. M. Shen, Z. C. Xu, T. Z. Yang and H.-J. Gao, *Chin. Phys. B*, 2008, **17**, 2066.
34 N. Hoshi, K. Kida, M. Nakamura, M. Nakada and K. Osada, *J. Phys. Chem. B*, 2006, **110**, 12480.
35 J. H. Chen, M. Y. Wang, B. Liu, Z. Fan, K. Z. Cui and Y. F. Kuang, *J. Phys. Chem. B*, 2006, **110**, 11775.
36 X. W. Yu and P. G. Pickup, *Electrochem. Commun.*, 2009, **11**, 2012.
37 S. Sharma, A. Ganguly, P. Papakonstantinou, X. P. Miao, M. X. Li, J. L. Hutchison, M. Delichatsios and S. Ukleja, *J. Phys. Chem. C*, 2010, **114**, 19459.
38 L. Dai and S. Z. Zou, *J. Power Sources*, 2011, **196**, 9369.

 